

Investigation of Transverse Relaxation Rate Distribution via Magnetic Resonance Imaging: Impact of Electrode Formation

Roland Balbierer,* Philipp Seegert, Sabrina Herberger, Thomas Wetzel, Hermann Nirschl, and Gisela Guthausen*

The impact of electrode formation is studied by the spatially and time-resolved distribution of transverse relaxation. In situ ^7Li nuclear magnetic resonance experiments are performed on an experimental lithium-ion battery cell to study the impact of electrode passivation via imaging and transverse relaxation in the interelectrode volume. The electrolyte in the battery, using technically relevant electrode material, i.e., graphite and lithium–nickel–cobalt–manganese–oxide, is studied by 2D magnetic resonance imaging. The electrolyte is 1 mol L^{-1} lithium hexafluorophosphate dissolved in a binary mixture of ethylene carbonate and dimethyl carbonate. 1D profiles are acquired and related to ^7Li concentration during passivation and during a constant current/constant voltage cycle. The transverse relaxation rate $R_2(z,t)$ measured by multiecho profiles revealed changes within the electrolyte volume. The ongoing process changes the relaxation distribution. Indications for a defective electrode passivation are deduced from the data. During one charging cycle with constant current/constant voltage, the lithium concentration is measured spatially resolved, and the data are modeled by the Nernst–Planck equation.

1. Introduction


Characterization of electrochemical systems is essential for reasonable input parameters of transport and mass transfer data for simulation models. The basis for an in-depth understanding of processes going on inside these systems is provided by the current state of the art analytical tools. Nuclear magnetic resonance (NMR) on electrochemical systems, especially on technical and commercially available lithium-ion batteries (LIBs), has to

deal with challenges due to the magnetism of the active material in cathodes and due to the skin-depth of radio frequency (RF). Therefore, the intrinsic demand of a nonmetallic but gas-tight cell enclosure persists. With respect to RF, various coil configurations are known. Volume coils provide a high signal-to-noise ratio (SNR) and good compatibility of equipment and electrochemical experimental cells, whereas other groups have used self-manufactured setups.^[1–13]

Investigations of LIB and their components via NMR and magnetic resonance imaging (MRI) have become very versatile, exploring diverse NMR-active nuclei, such as ^1H , ^7Li , ^{19}F , or ^{31}P .^[3,11,14–17] The impact of the orientation of the electrodes with respect to the static magnetic field B_0 and the RF field B_1 needs to be considered.^[15,18] The intercalation process of Li^+ into carbon-based anodes was measured by ^7Li NMR, using a Bellcore-type cell.^[19–22]

The studies were extended to lithium/silicon-based electrodes,^[23] as they are of current interest due to their significantly larger volumetric capacity, i.e., a factor of approximately 20. Single-Point Ramped Imaging with T_1 Enhancement (SPRITE) was applied to measure the intercalation of Li^+ into a graphite anode as a function of the state of charge (SOC).^[4] Furthermore, in operando experiments on cathode materials with lithium oxides were performed, where the cell voltage was related to the shifts in the ^7Li NMR spectra.^[7,24] Another important phenomenon on

R. Balbierer, Prof. H. Nirschl, Prof. G. Guthausen
Institute of Mechanical Process Engineering and Mechanics
Karlsruhe Institute of Technology (KIT)
Straße am Forum 8, D-76131 Karlsruhe, Germany
E-mail: roland.balbierer@kit.edu; gisela.guthausen@kit.edu

 The ORCID identification number(s) for the author(s) of this article can be found under <https://doi.org/10.1002/ente.202000579>.

© 2020 The Authors. Published by Wiley-VCH GmbH. This is an open access article under the terms of the Creative Commons Attribution-NonCommercial-NoDerivs License, which permits use and distribution in any medium, provided the original work is properly cited, the use is non-commercial and no modifications or adaptations are made.

DOI: 10.1002/ente.202000579

P. Seegert, S. Herberger, Prof. T. Wetzel
Institute of Thermal Process Engineering
Karlsruhe Institute of Technology (KIT)
Engelbert-Arnold-Straße 4, D-76131 Karlsruhe, Germany

Prof. G. Guthausen
Chair of Water Chemistry and Water Technology
Karlsruhe Institute of Technology (KIT)
Engler-Bunte-Ring 9a, D-76131 Karlsruhe, Germany

the surface of the electrodes is the formation of lithium microstructures, as they are related to the failed intercalation of Li^+ , whenever unsuitable operational parameters are chosen. Examples are too high or too low temperatures, combined with high charging/discharging rates, and when the potential of the graphite anode drops below 0 V. The shifts in the ^7Li NMR spectra, when lithium plating occurs, and the microstructural growth were investigated.^[13,14,25,26] Self-manufactured cylindrical cell casings with opposing electrode connections were used.^[3,4,7,9,13,27] Mass transfer or diffusion and ion concentration gradients in the electrolyte domain were described in the presence of applied potentials.^[1–3,6,9,26] Transport properties of charge carriers were characterized via inverse modeling, supplemented by NMR and MRI measurements.^[28] Bulk electrolytes were investigated by pulsed field gradient NMR (PFG-NMR) to determine diffusion coefficients for diverse electrolytes as a function of lithium salt and solvent concentration and temperature.^[2,29–32] Electrophoretic NMR was used to measure the ion transference number.^[33–35] In the cited investigations, different electrochemical systems with respect to electrolyte composition and active material have been used.

In this work, the focus is at first on a cell casing design with an external single-sided mounted electric contact, which allows for a relatively simple assembling of various electrode and electrolyte compositions especially inside a glove box. The sealing of the cell was realized by reusable material, and an option for adjustable interelectrode spacing was implemented. Second, 1D and 2D ^7Li MRI was performed on the electrode pair scale of an experimental LIB similar to refs. [6,9], whereas in this work the uncontrolled electrode passivation and the ion concentration were also studied in the electrolyte domain region during a constant current/constant voltage (CCCV) cycle.

2. Results and Discussion

2.1. In Situ 2D and 1D MRI

2D ^7Li MR images were acquired using the Multi Slice Multi Echo (MSME) pulse sequence. In the images of the experimental LIB cell, the electrolyte volume dominates the sagittal image. In addition, the bores for feedthrough of the soldered wire for electric connection can be identified on top and bottom of the image (Figure 2). The regions with lower signal intensity at the edges of the volume in transverse direction are due to the curvature of the cylindrical sample volume. Furthermore, the structure of the separator stack is visible consisting of 12 layers. The copper disk can be identified at approximately $z = 14$ mm, and the aluminum disk at approximately $z = 4$ mm. The head part of the cell for an aimed electrode spacing of 10 mm was used, with a separator and electrode diameter of 12.5 mm. The 2D ^7Li MR images were acquired using frequency encoding along y and phase encoding along z . The complete measurement time was 15 h comprising 128 accumulations at $T_R = 4.7$ s.

1D ^7Li profiles were measured to investigate the electrolyte volume with respect to critical conditions, i.e., electrode formation: no formation cycle was performed after assembly and therefore intentionally, no solid electrolyte interface (SEI) was built up. The impact of this formation procedure is well known, as Li^+ transport is allowed while electron impermeability is provided,

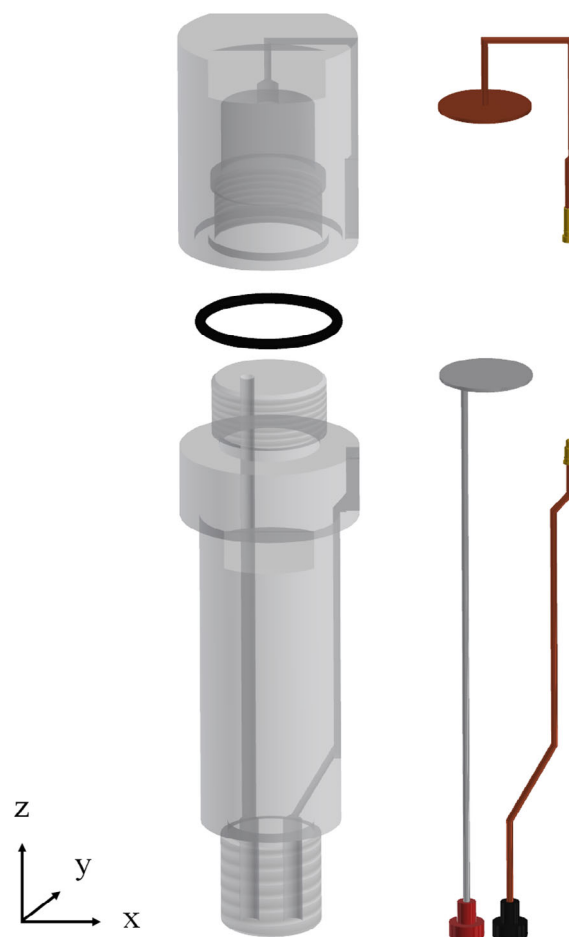


Figure 1. Schematic drawing of the cell casing with separated electric and mechanical components as well as sealing (left). The transparent illustration shows the location of electric paths and the electrochemical cell. On the right, the electric connectors and the current carrying paths are shown separately. Bores were closed by a two-component adhesive.

but it is difficult to be addressed experimentally.^[36] During the MRI investigations no current was applied, and the open-circuit voltage (OCV) was measured simultaneously. The absence of an SEI in combination with the low cell voltage after assembly leads to a chemical decomposition, where the chemical reactions involve the electrodes, solvent molecules, and ions.^[36]

The profiles were measured along z (orientation defined in **Figure 1**), the axis perpendicular to the electrodes (**Figure 2**) while the signal in the xy -plane was averaged according to the chosen slice selection. A total of 1380 z -profiles were acquired and subsequently automatically processed as a function of time every approximately 10 min (**Figure 3**), each consisting of 64 accumulated NMR experiments with 16 separately acquired echoes.^[37] The anode was located at approximately $z = 12$ mm and the cathode at approximately $z = 2$ mm. In **Figure 3** every 60th profile is displayed for reasons of clarity. Blurring of the intensity profiles is negligible, as a single experiment time, i.e., 10 min, provided sufficient time to capture small intensity changes while simultaneously providing an adequate time resolution for the processes going on.

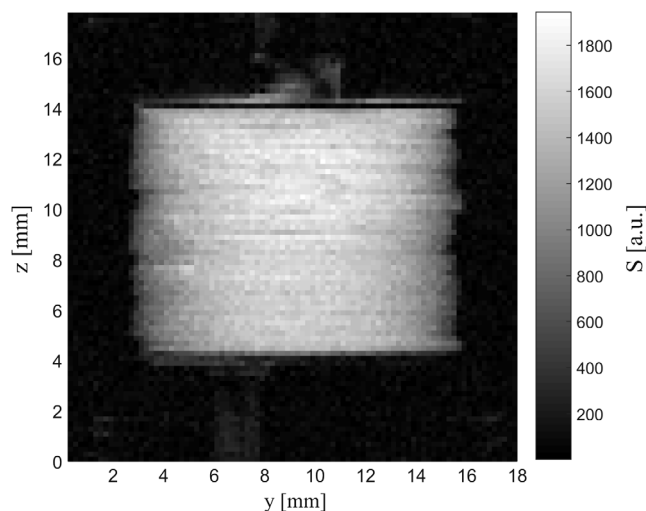


Figure 2. 2D ^7Li MR sagittal image of an experimental LIB, acquired with MSME averaging over 16 echoes. A homogeneous electrolyte distribution in the separator stack and the location of current collector connecting disks can be seen. The signal S decreases toward the cell edges (small and large y -values), which is due to the cylindrical shape of the cell in combination with the large slice thickness chosen in the experiment.

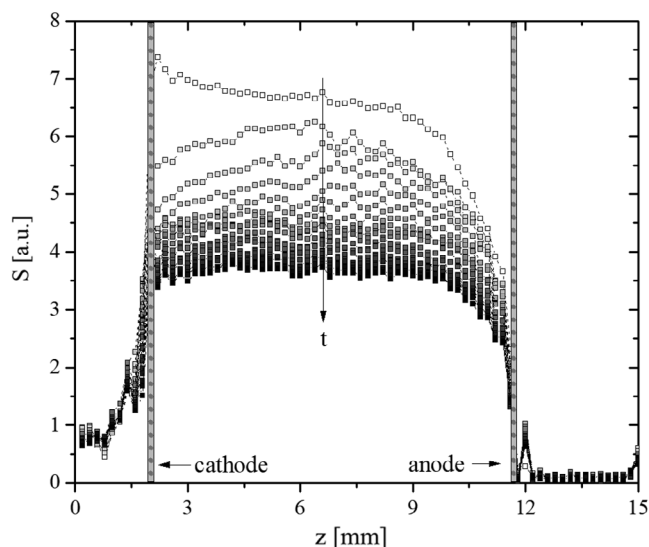


Figure 3. 1D ^7Li z -profiles, each acquired within a measurement time of 10 min. The signal intensity of the first echo at an echo time τ_E of 2.7 ms is displayed. For reasons of clarity, only every 60th profile of the acquired data set is shown to describe signal intensity decrease as a function of time in the interval $[0, 250]$ h. The positions of electrodes are marked. Dotted lines are guides for the eye. An unequal distribution of Li^+ at small t is observed, which levels with experiment time. The signal intensity in the electrolyte volume significantly decreases as the relaxation properties change due to an autonomous passivation process. This is explained in the text in more detail.

In the regions close to both electrodes, different processes characterized by individual time scales are evident in that respective time series of z -profiles, and have a major impact on the ^7Li NMR signal. The overall MSME signal declines over time. Physically, Li^0 or Li^+ cannot get lost, nor leave the cell, except for potential leakage. The avoidance of the latter was a strict

requirement of the cell itself and was proven prior to the MRI experiment. Therefore, it is to be excluded as an explanation. Nevertheless, the profiles indicate that the concentration of Li^+ in the electrolyte volume decreases with time, if not the NMR properties of the Li^+ themselves change. This would be the case in the presence of dominant quadrupolar or hyperfine transverse relaxation, and to a lower extent to fluctuations of dipolar couplings. These factors will be discussed in more detail later.

2.2. Transverse Relaxation $R_2(z,t)$

R_2 was measured by acquiring 16 echoes in the 1D MSME experiments, which allowed to extract the signal intensities as a function of $n \times \tau_E$ with $n \in [1, 16]$. The echo decay was modeled by an exponential decay in accordance to Bloch's equations, resulting in $R_2(z,t)$ as a function of z and t (Figure 4a). At the beginning of the experiment, a rather homogeneous distribution along z in the range $R_2 \in [1, 4] \text{ s}^{-1}$ was observed. $R_2(z,t)$ considerably increases with t . After $t > 6$ h, i.e., after the time of reversal of the cell voltage, the increase becomes dominant near the cathode, whereas comparatively lower values are observed toward the anode (Figure 4a). At $t = 523$ h, a reverse behavior is observed. In summary, the data show a strong increase in R_2 up to $R_2 \approx 100 \text{ s}^{-1}$. For the first period up to 80 h, this coincides with the monotonous decrease in the OCV, which approaches the minimum voltage $U = -2.023 \text{ V}$ after approximately 80 h (Figure 4b). A detailed analysis of $R_2(z,t)$ revealed a rather constant and homogenous distribution along z until the reversal of the cell voltage at approximately $t = 6$ h. Starting from there, the relaxation rate increases for all z -values while showing prominent changes at small z . After $t = 11$ h, an intense gradient $\frac{dR_2}{dt}$ was found for cathode near z -values, while $U \approx -1.8 \text{ V}$. An exponential decrease in the cell voltage was observed, until a plateau value was reached, i.e., up to 100 h.

The function

$$U(t) = 2.914 \text{ V} \times \exp(-0.0561 \text{ h}^{-1} \times t) - 2.030 \text{ V} \quad (1)$$

describes the voltage $U(t \leq 100 \text{ h})$ well, with $R^2 = 0.999$ and a root mean squared error $\text{RMSE} = 0.7\%$. The exponentially modeled decrease in the cell voltage can be attributed to the continuous passivation of both electrodes and the chemical decomposition of the electrolyte solvents. The occurring high potential at the anode is known to cause oxidation of the copper current collector and a decomposition of the electrolyte solvents into radicals and gases.^[36] The low potential at the cathode, on the contrary, generally facilitates an electrophoretic deposition of copper ions on this side of the electrochemical cell. This effect mainly would have been seen as gradients of R_2 near the anode. The large gradient of R_2 around $z = 2 \text{ mm}$ indicates a process starting at the cathode pointing on a slow detachment of paramagnetic material of the lithium–nickel–manganese–cobalt-oxide (NMC) cathode. In addition, but not significant for the acceleration of transverse relaxation, impurities in the electrolyte are known to react with electrolyte components to form products such as HF or CO_2 .^[36,38–44]

The cell voltage is a macroscopic measure of these processes; in the following, the microscopic view of ^7Li NMR will be discussed. The signal attenuation in the 1D profiles (Figure 3)

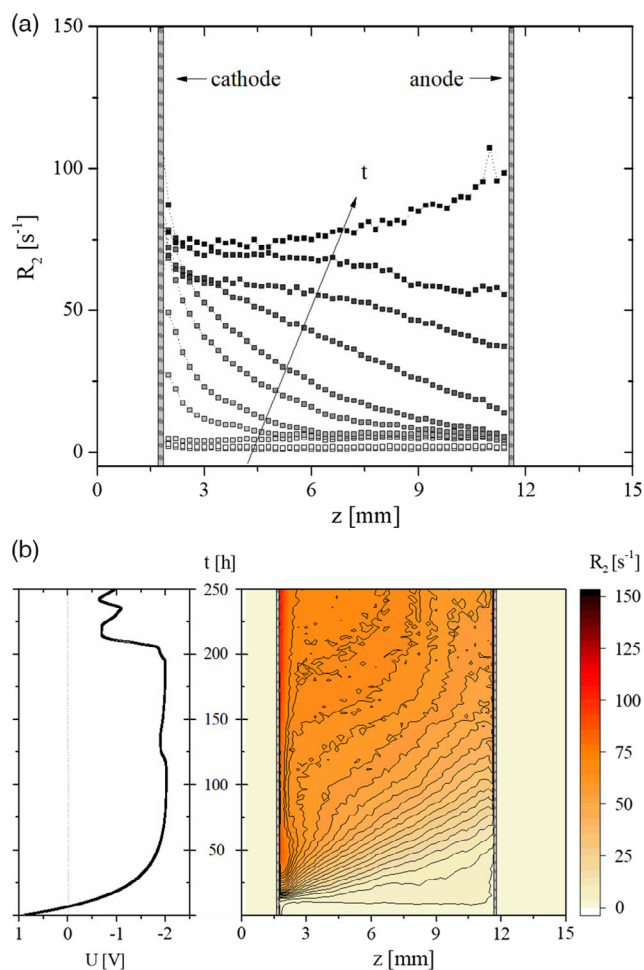


Figure 4. a) Profiles of the transverse relaxation rate $R_2(z,t)$ along z and as a function of time t . For reasons of clarity eleven selected profiles at different t are shown at $t = 0, 5, 11, 16, 21, 32, 43, 68, 115, 244,$ and 523 h. The electrode locations are depicted by gray bars. b) Contour plot of $R_2(z,t)$ showing its significant increase over the entire electrolyte volume. The open-circuit cell voltage was measured simultaneously indicated by the coupled time axis: voltage decreases to minimum $U = -2.023$ V. A polarity reversal appears after approximately 6 h, together with the nonuniform profiles of $R_2(z,t)$. These observations indicate a significant change in chemical composition in the electrolyte volume.

can be attributed to two main factors: 1) drastically enhanced transverse relaxation, due to formation or relocation in the electrochemical cell and 2) formation of other Li chemical compounds. Therefore, in addition ^7Li NMR spectra were acquired to shorten the time until observation considerably to roughly $50 \mu\text{s}$, which is the dead time of the probe, instead of the 2.7 ms echo time in MSME. The intensities of the spectra with only one considerable peak and the echo images were back-extrapolated to zero echo time and compared. The ratio of the integrated signal intensity in NMR spectroscopy was determined to be $\frac{S(t=258.4\text{h})}{S(t=0\text{h})} \approx 70\%$ while keeping the acquisition parameters constant. This agrees with the findings in the 1D ^7Li profiles (intensities back-extrapolated to $\tau_E = 0$ ms): $\frac{S(t=258.2\text{h})}{S(t=0\text{h})} \approx 65\%$ (Figure 3).

This apparent loss of ^7Li signal intensity implies that other Li chemical compounds and environments must have been formed. This is also indicated, but not fully explained by the recognized increase in linewidth. The full width at half maximum (FWHM) for the first experiment was $FWHM = 0.86$ ppm. Broadening of the ^7Li peak of the LiPF_6 electrolyte species was quantified to a maximum of $FWHM = 1.44$ ppm, but no additional lines at any shift in the range of ± 6000 ppm were observed. In NMR on nanoparticles it is known that these structures lead to a linewidth of several hundreds of ppm instead of a few ppm.^[45] Therefore, disordered structures or magnetic structures like NMC containing Li^+ or Li^0 are assumed to lead to very broad linewidths and simultaneously rather low signal intensities. These signal contributions will vanish in the unavoidable experimental noise of the NMR spectrometer and are the most likely explanation for the observation of the $\approx 30\%$ decrease in ^7Li signal.

The other observation to be addressed in more detail is the drastic increase in R_2 of ^7Li with $I = 3/2$. Two reasons are to be discussed: quadrupolar and hyperfine relaxation. As ^1H with nuclear spin $I = 1/2$ is insensitive to quadrupolar effects unlike ^7Li , ^1H -NMR was performed at certain times to shed some light onto this question. Only the solvent molecules in the electrolyte and their signals are considered in ^1H -NMR, i.e., ethylene carbonate (EC) and dimethyl carbonate (DMC). The ^1H -NMR measurements were performed at $t \approx 526$ h, and the result matched with the findings of ^7Li MRI (Figure 4a): a homogeneous distribution of $R_2(^1\text{H})$ along z at values of $R_2(^1\text{H}) \in [90, 100] \text{ s}^{-1}$ was measured, with increasing values toward the anode (Figure 5). In pristine electrolyte, $R_2(^1\text{H})$ is in the order of $0.5\text{--}2 \text{ s}^{-1}$. In comparison, the ^7Li relaxation rate at $t = 523$ h amounted to $R_2(^7\text{Li}) \in [80, 100] \text{ s}^{-1}$, showing the same trend of larger values toward the anode. The similarity of the findings in ^1H and ^7Li transverse relaxation indicates that the ^7Li transverse relaxation is continuously enhanced, mainly due to hyperfine relaxation. This effect is

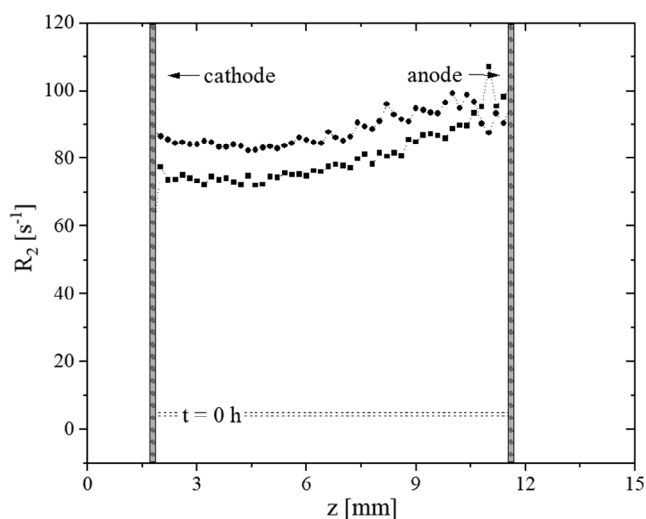


Figure 5. Comparison of the transverse relaxation rates $R_2(z,t)$ for the ^7Li (■) and ^1H (●) experiments at $t = 523$ h and $t = 526$ h, respectively. High values for R_2 at the end of the experiment and similar behavior with increasing R_2 toward the anode can be observed. The dotted lines represent $R_2(t = 0 \text{ h})$ for both species at $R_2(^7\text{Li}) \in [1, 4] \text{ s}^{-1}$ and $R_2(^1\text{H}) \in [0.5, 2] \text{ s}^{-1}$.

well known in NMR as paramagnetic relaxation enhancement (PRE): (super-)paramagnetic particles enhance transverse relaxation via their fluctuating magnetic fields.^[46,47] It should be mentioned that the relaxation enhancement is directly proportional to concentration, provided a single component or species contributes to PRE. The measurements indicate that magnetic compounds, ions, (nano-) particles, or other moieties are increasingly present in the electrolyte volume, most probably originating from the active material of the cathode, which is known to be strongly magnetic and indicated by the gradient of $R_2(z,t)$ at $z = 2$ mm. Apart from the concentration gradient of these materials along z being evident in the R_2 profiles, the unusually large potential at the anode provides an additional driving force for the reallocation in the entire electrolyte volume. Furthermore, the increase in $R_2(^7\text{Li})$ along z at the end ($t = 523$ h) can be explained by the continuous accumulation of paramagnetic cathode material as the voltage remains reversed.

2.3. CCCV Cycle and Modeling

The experimental LIB cell was further investigated by in situ 1D ^7Li MRI during a CCCV cycle (Figure 6) subsequent to the discussed OCV phase. The focus was on the concentration gradients of charge carriers during charging while having demonstrated that autonomous processes with possible electrochemical disabling nature. As previous studies showed that the concentration gradient across the interelectrode volume depends on the amplitude of the charging current and on temperature and is observable by ^7Li , ^{19}F , or ^{31}P MRI.^[1,3-6,9,28] In contrast to these studies, the concentration profiles during CCCV in this work were investigated in a ^7Li MRI birdcage, which allowed for an electrode

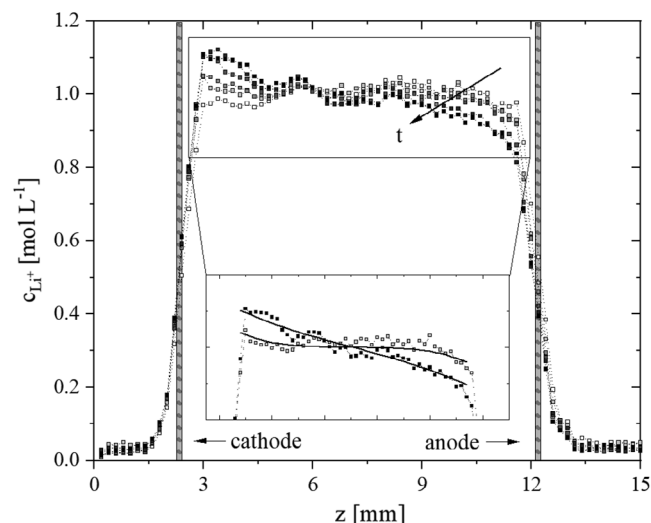


Figure 6. Li^+ concentration profiles during the CCCV phase along the interelectrode distance z at $t = 0, 1.8, 3.8, 5.9, 8.9,$ and 11.6 h, respectively. For reasons of clarity only six profiles are shown, which were denoised via a moving average over five points. The location of the electrodes is again indicated by gray bars. The modeling via Nernst–Planck equation under consideration of mass conservation (inset, solid lines) describes the measured data well, as shown by the two concentration profiles at 1.8 and 11.6 h in the inset.

diameter of 12.5 mm while using the aforementioned cell with the prior defective passivation of the electrodes. The measured profiles indicate the ^7Li concentration gradients along z also in this case (Figure 6).

The electrolyte diffusion coefficient D_E for the used electrolyte was calculated via the harmonic mean of the ion diffusion coefficients $D(\text{Li}^+) = 2.61 \times 10^{-10} \text{ m}^2 \text{ s}^{-1}$ and $D(\text{PF}_6^-) = 4.02 \times 10^{-10} \text{ m}^2 \text{ s}^{-1}$ to $D_E = \frac{2 \cdot D(\text{Li}^+) \cdot D(\text{PF}_6^-)}{D(\text{Li}^+) + D(\text{PF}_6^-)} = 3.17 \times 10^{-10} \text{ m}^2 \text{ s}^{-1}$.

The values for the ion diffusion coefficient were determined in separate ^7Li and ^{19}F PFG-NMR experiments at 30°C with a stimulated echo pulse sequence consisting of 16 gradient steps with a gradient duration of $\delta = 2$ ms, a diffusion time $\Delta = 100$ ms, and a repetition time of $T_R = 5$ s. In the battery cell, porosity ϵ and tortuosity τ need to be considered as glass fiber separators are present and influence diffusion. ϵ and τ were set to common values for the used separator material,^[48,49] whereas τ was also determined experimentally in several ^7Li PFG-NMR experiments. The result is in a comprehensible range and amounted to $\frac{\epsilon}{\tau} = \frac{0.8}{1.2} = 0.67$, which results in the effective electrolyte diffusion coefficient $D_{E,\text{eff}} = \frac{\epsilon}{\tau} \times D_E$. The basis for modeling $\frac{\partial c(z,t)}{\partial t}$ is the Nernst–Planck equation under consideration of mass conservation (Equation (2))

$$\frac{\partial c(z,t)}{\partial t} = \frac{\partial}{\partial z} \left[D_{E,\text{eff}} \frac{\partial c(z,t)}{\partial z} + \frac{i(1-t^+)}{FA} \right] \quad (2)$$

The ion fluxes are induced by the current i for the single electrode surface area A corresponding to the electrode diameter $d = 12.5$ mm. The transference number t^+ accounts for the ratio of the Li^+ contribution to the overall electric conductivity of the electrolyte. $t^+ = 0.30$ was used for parameterization of Equation (2).^[3] F is the Faraday constant.

The steady-state condition (Equation (3)), where

$$-D_{E,\text{eff}} \frac{\partial c}{\partial z} = \frac{i(1-t^+)}{FA} \quad (3)$$

was almost reached during the CV phase, as indicated by negligible change of $\frac{\partial c}{\partial t}$ after $t = 11.6$ h. Hence, the concentration c approaches a time-constant behavior, and shows an approximately linear relation along z ,^[1,3] as indicated by the final concentration profile at 11.6 h (Figure 6). The CC threshold of 4.1 V and the CV threshold of $5 \mu\text{A}$ were reached at 9.4 and 11.5 h, respectively. The buildup of the steady-state condition ranged over the entire CCCV phase. The physically interesting quantity is the ^7Li concentration, which can be estimated from the 1D profiles by $c(z,t) = \frac{S(z,t)}{S_0} \times c_0$ at the smallest echo time, i.e., the first echo image. The initial lithium salt concentration in the electrolyte was $c_0 = 1 \text{ mol L}^{-1} \text{ LiPF}_6$. The signal in the 1D profiles was normalized to S_0 , which was the mean intensity over $n = 44$ data points in the first profile, i.e., $S_0 = \frac{1}{n} \sum_{i=1}^n S(i, t = 0)$. It should be mentioned that this procedure neglects the signal decrease during the OCV phase mentioned before. Furthermore, an exact relation of signal intensity to ion concentration requires knowledge of the concentration-dependent relaxation rate $R_2(c, t)$ of the investigated system. This normalization is to be seen as an indication—how strong the lithium concentration changes due to a defined

charging current under the mentioned experimental conditions. It cannot be quantitatively compared with other studies without prior determination of relaxation. The normalization therefore is a first approach to relate signal intensity to the known initial salt concentration. The approximate position of the electrodes is $z = 2$ mm for the cathode and $z = 12$ mm for the anode as indicated by the gray bars in Figure 6. The field of view (FOV) and therefore the position slightly changed with respect to, e.g., Figure 3. This is due to the repeated insertion of the cell into the probe. The concentration maxima at cathode and anode sides at $t = 11.6$ h amounted to $c_{\text{cathode}} = 1.107 \text{ mol L}^{-1}$ and $c_{\text{anode}} = 0.893 \text{ mol L}^{-1}$, respectively, which are larger than expected when compared with similar work.^[6,9] Nevertheless, the concentrations agree with the reduced charge carrying surface due to the defective passivation beforehand, even at such a low current density, i.e., $i/A = 0.5 \text{ A m}^{-2}$. Equation (2) describes the experimental data, when scaling the value of active, current carrying surface area empirically by a factor of 1/60. This is well explained by the defective passivation during the long-term OCV phase, and therefore less surface area on the electrodes is available for charge transfer. For the second CCCV cycle, the CC threshold of 4.1 V was reached directly after applying the constant current, which means a complete disabling of the electrodes occurred within the given voltage window.

Another indication was obtained after the NMR/MRI experiments including the CCCV cycle: a high inner pressure was observed as the electrolyte sprayed off from the sealing surface in the first moment of opening the cell. Moreover, an extensive detachment of the active material on the cathode and a reddish discoloration indicating Cu^1 ions, with increasing saturation toward the cathode, were observed. The latter is attributed to a general degradation of the copper current collector at the high electric potential at the anode in combination with the reversed cell voltage, corresponding to an electromagnetic field forcing positively charged ions toward the cathode. The combination of excessive change in the transverse relaxation rate $R_2(z,t)$ in the electrolyte volume (Figure 3) and the findings in the onetime CCCV cycle afterward (Figure 6) lead to the conclusion that formation seen in macroscopic measures, e.g., voltage and voltage reversal, can be correlated to microscopic measures. Via the transverse relaxation rate, the change in the electrolyte composition and the decomposition of electrode material was observed on the microscopic level experimentally. The defective passivation becomes evident by the large concentration gradients (Figure 6) measured by MRI during the CCCV cycle at rather low current density for the used electrode diameter. Reaction kinetics in different electrochemical systems can therefore be investigated with the described experimental setup.

3. Conclusion

The presented cell design for in situ investigations of electrochemical systems via NMR/MRI and other techniques provides proper and stable sealing while allowing the interelectrode spacing to be easily adjusted. The electric connectivity and reusability of the parts is maintained, which outlines the main advantage of the presented design. Spin-echo-based 2D MRI and 1D profiles were performed on an experimental LIB, containing application-

orientated electrode materials and electrolytes, i.e., graphite and NMC with 1 mol L^{-1} LiPF_6 in EC/DMC (1:1, v:v). Modeling methods for the interelectrode ion concentration gradient can be extended by the transport parameters extracted from experimental data, e.g., during a CCCV cycle. A novel approach to study the impact of electrode formation is provided by the spatially and time-resolved distribution of the transverse relaxation rate $R_2(z,t)$, while also the signal intensity is considered to be a function of experiment time. Furthermore, the presented method enables investigations of the stability of liquid electrolytes used in electrochemical systems via transverse relaxation rate, which was found to be mainly determined by paramagnetic relaxation enhancement. Finally, and as a perspective, reaction kinetics and concentration determination can be studied by NMR with the presented cell casing.

4. Experimental Section

Design of Cell Casing: The cell casing (Figure 1) was designed and manufactured in-house from polyether ether ketone (PEEK) as it provides sufficient long-term chemical resistance for the applied electrolyte.^[8] An inner metric fine pitch thread was used at the head, i.e., the location of the electrochemical system. The intension was to withstand the tightening, while a small front surface for potential electrolyte flow from the cell toward the sealing is provided. As per requirement of the birdcage the outer diameter of the casing was 25 mm, whereas the inner diameter was 13 mm. The electrode materials and separators were prepared with diameters of 12.5 mm, to allow potential gas enclosures not to be trapped and to escape toward the sealing at the edges of the cell volume. The length of the casing was 90 mm to accommodate the necessary distance between the homogeneity center of B_1 and the electric terminal sockets. Standard 1 mm terminal socket connectors with gold plated contact surface were used to minimize ohmic losses at the contact interfaces. The design comes with an external, single-side mounted current collector contact, surrounded by a standard thread for positioning. Moreover, with the used connection disks, i.e., 300 μm -thick copper for anode and aluminum for cathode, mixed potentials on the interfaces are avoided. The spring-loaded connector and counterpart between head and screw of the cell provided similar electrical properties, i.e., both were gold plated, and enabled electric connection independent from rotation during assembling. All connections have been soldered. The spring-loaded connector was installed in the bottom part to realize the required distance from the sensitive region of the MRI probe. The sealing of the cell was done with a single fluoroelastomer (FPM) O-ring and therefore avoids single-use cutting ring seals. All bores were closed using two-component adhesive Araldite 2014-2, which empirically provides sufficient chemical resistance and low porosity. An adjustable electrode spacing is realized by an exchangeable head part of the cell and is independent from sealing and the electrical connections. The assembly of the cell was performed inside a glove box.

Cell Preparation and Materials: 1 mol L^{-1} LiPF_6 -based electrolyte was purchased from Sigma-Aldrich, whereas the organic solvents were EC and DMC in a 1:1 volume ratio. The solution was used as received and handled under an argon atmosphere while monitoring O_2 and H_2O concentrations. Whatman glass fiber membranes were purchased as separators from Sigma-Aldrich, namely, GF/D with a mean pore size of 2.7 μm . The graphite and NMC electrode material were purchased from Custom Cells, Itzehoe, Germany and used as received. Both provided high power characteristics according to electrode composition, i.e., layer thickness and amount of binder and conductive additives. All bulk materials and cell casing parts, excluding the aluminum bottles containing electrolyte and the sealed electrodes, were dried for at least 24 h in a vacuum oven at 80 °C prior to insertion into the glove box. The electrodes were placed inside the cell casing, starting with anode, into the screwable head part with inner thread. When placing 12 Whatman GF/D separators

subsequently, the stack was found to be more aligned when compressing each layer individually after insertion. Before placing the cathode, 1.1 mL of electrolyte was filled in, i.e., 1 mol L⁻¹ LiPF₆ in EC/DMC (1:1, v:v) (Figure 1). To avoid damage of the permanent parts, e.g., damages on connection faces of the cell, thin copper (on the anode side) and aluminum foil (on the cathode side) were used as intermedia layers. The foil thickness varied, but did not exceed 25 μm. With these assembly settings, air tightness was achieved, reusability of all casing parts was realized, and sufficient chemical resistance was provided. The compression due to the thread, while closing the cell by turning the bottom part upside down inside the head part, was sufficient to distribute the electrolyte homogeneously. No gas locks in the separator stack were observed and a valid ionic connection between electrodes across the entire volume and electrode diameter was provided.

MRI Experiments: A MSME pulse sequence was used for all MRI experiments. ⁷Li and ¹H were measured at Larmor frequencies of 77.75 and 200.07 MHz, respectively (Bruker 200 MHz Avance III HD spectrometer). Commercial birdcages with a maximum sample diameter of 25 mm were used in quadrature mode for ¹H and in linear mode for ⁷Li, mounted on MICWB40 probe basis. The maximum gradient was 1.5 T m⁻¹. The software ParaVision 6 controlled the spectrometer. The minimum spatial resolution amounted to 200 μm in the ⁷Li MR images. The FOV was 18 × 18 mm × mm in the yz 2D images (Figure 2) and 15 mm for the z-profiles (e.g., Figure 3), at a slice thickness of 18 mm in x-direction, and 15 mm in the xy-plane, respectively. The complete inner cylindrical volume of the cell was thus measured. Sixteen echo images were acquired and averaged in the 2D MSME experiments. The echo time τ_E was chosen to 3.2 and to 2.7 ms for 2D and 1D MRI, respectively. The spatially resolved relaxation rate R₂(z) = 1/T₂(z) was investigated by acquiring each of the echoes separately. The repetition times were T_R ≈ 5 s because T₁ was independently determined to T₁ = 1 s for 1 mol L⁻¹ LiPF₆ in EC/DMC (1:1, v:v).

Electric Connections and Cycling: A PalmSens 4 galvanostat/potentiostat was used for the CCCV cycle, with 60 μA as current set point during the CC phase, which equaled to 0.5 A m⁻² with respect to electrode diameter of 12.5 mm. The cutoff voltage for the transition to the CV phase was set to 4.1 V, a typical value for NMC. A current limit of 5 μA was set as threshold to terminate the CV phase. The connection was conducted by a double shielded, twisted pair cable, supplemented by a low-pass filter for each DC line to reduce electromagnetic pickup along the electric connection. The cable length was kept to a maximum of 5 m to avoid noise pickup influencing the NMR signal quality.

Acknowledgements

The authors thank the German Research Foundation (DFG) for financial support of the instrumental facility Pro²NMR and for the MR instrumentation. Funding and the cooperative support within GRK 2218: SIMET – Simulation of Mechanical, Electrical, and Thermal properties of lithium-ion batteries, project number 281041241, is acknowledged as well. Furthermore, the discussions with Jonathan David Bazak from the McMaster University, Canada, and the colleagues from Pro²NMR, namely, Nicolas Schork, Sebastian Schuhmann, and Thomas Rudzuck at KIT are acknowledged. The cooperation and support by Sabine Paarmann and Oliver Queisser from the Institute of Thermal Process Engineering (TVT) and by Rainer Mönig, Dominik Kramer, and Manfred Janzen from the Institute of Applied Materials (IAM-WBM) from KIT are highly appreciated. The authors thank the technical facilities at the Institute of Mechanical Process Engineering and Mechanics (MVM), namely, Olaf Jörg, for the manufacturing of the cell casing. Open access funding was enabled and organized by Projekt DEAL.

Conflict of Interest

The authors declare no conflict of interest.

Keywords

electrochemistry, ion concentration distributions, lithium-ion batteries, nuclear magnetic resonance, solid electrolyte interfaces

Received: June 21, 2020

Revised: July 24, 2020

Published online:

- [1] J. D. Bazak, S. A. Krachkovskiy, G. R. Goward, *J. Phys. Chem. C* **2017**, *121*, 20704.
- [2] S. A. Krachkovskiy, J. D. Bazak, S. Fraser, I. C. Halalay, G. R. Goward, *J. Electrochem. Soc.* **2017**, *164*, A912.
- [3] S. A. Krachkovskiy, J. D. Bazak, P. Werhun, B. J. Balcom, I. C. Halalay, G. R. Goward, *J. Am. Chem. Soc.* **2016**, *138*, 7992.
- [4] S. A. Krachkovskiy, J. M. Foster, J. D. Bazak, B. J. Balcom, G. R. Goward, *J. Phys. Chem. C* **2018**, *122*, 21784.
- [5] S. A. Krachkovskiy, A. D. Pauric, I. C. Halalay, G. R. Goward, *J. Phys. Chem. Lett.* **2013**, *4*, 3940.
- [6] S. Klamor, K. Zick, T. Oerther, F. Schappacher, M. Winter, G. Brunklaus, *Phys. Chem. Chem. Phys.* **2015**, *17*, 4458.
- [7] E. Salager, V. Sarou-Kanian, M. Sathiy, M. Tang, J.-B. Leriche, P. Melin, Z. Wang, H. Vezin, C. Bessada, M. Deschamps, *Chem. Mater.* **2014**, *26*, 7009.
- [8] S. A. Kayser, A. Mester, A. Mertens, P. Jakes, R.-A. Eichel, J. Granwehr, *Phys. Chem. Chem. Phys.* **2018**, *20*, 13765.
- [9] M. Klett, M. Giesecke, A. Nyman, F. Hallberg, R. W. Lindström, G. r. Lindbergh, I. n. Furó, *J. Am. Chem. Soc.* **2012**, *134*, 14654.
- [10] S. Wiemers-Meyer, M. Winter, S. Nowak, *Phys. Chem. Chem. Phys.* **2017**, *19*, 4962.
- [11] S. Chandrashekar, N. M. Trease, H. J. Chang, L.-S. Du, C. P. Grey, A. Jerschow, *Nat. Mater.* **2012**, *11*, 311.
- [12] R. E. Gerald, J. Sanchez, C. S. Johnson, R. J. Klingler, J. W. Rathke, *J. Phys.: Condens. Matter* **2001**, *13*, 8269.
- [13] F. Poli, J. S. Kshetrimayum, L. Monconduit, M. Letellier, *Electrochem. Commun.* **2011**, *13*, 1293.
- [14] A. J. Ilott, M. Mohammadi, H. J. Chang, C. P. Grey, A. Jerschow, *Proc. Natl. Acad. Sci. U.S.A.* **2016**, *113*, 10779.
- [15] N. M. Trease, L. Zhou, H. J. Chang, B. Y. Zhu, C. P. Grey, *Solid State Nucl. Magn. Reson.* **2012**, *42*, 62.
- [16] N. Dupré, J. Oliveri, J. Degryse, J.-F. Martin, D. Guyomard, *Ionics* **2008**, *14*, 203.
- [17] C. P. Grey, N. Dupré, *Chem. Rev.* **2004**, *104*, 4493.
- [18] I. Serša, U. Mikac, *J. Magn. Reson.* **2018**, *294*, 7.
- [19] F. Chevallier, M. Letellier, M. Morcrette, J.-M. Tarascon, E. Frackowiak, J.-N. Rouzaud, F. Béguin, *Electrochem. Solid-State Lett.* **2003**, *6*, A225.
- [20] F. Chevallier, F. Poli, B. Montigny, M. Letellier, *Carbon* **2013**, *61*, 140.
- [21] M. Letellier, F. Chevallier, M. Morcrette, *Carbon* **2007**, *45*, 1025.
- [22] J.-M. Tarascon, A. Gozdz, C. Schmutz, F. Shokoohi, P. Warren, *Solid State Ion.* **1996**, *86*, 49.
- [23] B. Key, R. Bhattacharyya, M. Morcrette, V. Seznec, J.-M. Tarascon, C. P. Grey, *J. Am. Chem. Soc.* **2009**, *131*, 9239.
- [24] K. Shimoda, M. Murakami, D. Takamatsu, H. Arai, Y. Uchimoto, Z. Ogumi, *Electrochim. Acta* **2013**, *108*, 343.
- [25] H. J. Chang, A. J. Ilott, N. M. Trease, M. Mohammadi, A. Jerschow, C. P. Grey, *J. Am. Chem. Soc.* **2015**, *137*, 15209.
- [26] H. J. Chang, N. M. Trease, A. J. Ilott, D. Zeng, L.-S. Du, A. Jerschow, C. P. Grey, *J. Phys. Chem. C* **2015**, *119*, 16443.
- [27] S. Klamor, K. Zick, T. Oerther, F. M. Schappacher, M. Winter, G. Brunklaus, *Phys. Chem. Chem. Phys.* **2015**, *17*, 4458.

- [28] A. K. Sethurajan, S. A. Krachkovskiy, I. C. Halalay, G. R. Goward, B. Protas, *J. Phys. Chem. B* **2015**, *119*, 12238.
- [29] K. Hayamizu, *Annual Reports on NMR Spectroscopy* (Ed: G. A. Webb), Academic Press, Cambridge, MA **2019**, p. 57.
- [30] J. Peng, M. Gobet, M. Devany, K. Xu, A. von Wald Cresce, O. Borodin, S. Greenbaum, *J. Power Sources* **2018**, *399*, 215.
- [31] Z. Feng, K. Higa, K. S. Han, V. Srinivasan, *J. Electrochem. Soc.* **2017**, *164*, A2434.
- [32] P. Porion, Y. R. Dougassa, C. Tessier, L. El Ouatani, J. Jacquemin, M. Anouti, *Electrochim. Acta* **2013**, *114*, 95.
- [33] M. Gouverneur, J. Kopp, L. van Wüllen, M. Schönhoff, *Phys. Chem. Chem. Phys.* **2015**, *17*, 30680.
- [34] M. Brinkkötter, G. A. Giffin, A. Moretti, S. Jeong, S. Passerini, M. Schönhoff, *Chem. Commun.* **2018**, *54*, 4278.
- [35] M. P. Rosenwinkel, M. Schönhoff, *J. Electrochem. Soc.* **2019**, *166*, A1977.
- [36] A. Wang, S. Kadam, H. Li, S. Shi, Y. Qi, *NPJ Comput. Mater.* **2018**, *4*, 15.
- [37] R. Balbierer, R. Gordon, S. Schuhmann, N. Willenbacher, H. Nirschl, G. Guthausen, *J. Mater. Sci.* **2019**, *54*, 5682.
- [38] A. Guéguen, D. Streich, M. He, M. Mendez, F. F. Chesneau, P. Novák, E. J. Berg, *J. Electrochem. Soc.* **2016**, *163*, A1095.
- [39] R. Guo, L. Lu, M. Ouyang, X. Feng, *Sci. Rep.* **2016**, *6*, 30248.
- [40] T. Kawamura, S. Okada, J.-i. Yamaki, *J. Power Sources* **2006**, *156*, 547.
- [41] E. J. Nemanick, D. Wang, J. Matsumoto, N. Ives, Meeting Abstracts, MA2016-02, 897, **2016**.
- [42] A. V. Plakhotnyk, L. Ernst, R. Schmutzler, *J. Fluorine Chem.* **2005**, *126*, 27.
- [43] M. Stich, M. Göttlinger, M. Kurniawan, U. Schmidt, A. Bund, *J. Phys. Chem. C* **2018**, *122*, 8836.
- [44] K. Tasaki, K. Kanda, S. Nakamura, M. Ue, *J. Electrochem. Soc.* **2003**, *150*, A1628.
- [45] K. Märker, P. J. Reeves, C. Xu, K. J. Griffith, C. P. Grey, *Chem. Mater.* **2019**, *31*, 2545.
- [46] I. Bertini, C. Luchinat, G. Parigi, *Solution NMR of Paramagnetic Molecules: Applications to Metallobiomolecules and Models*, Elsevier Science B.V., Amsterdam **2001**, p. 372.
- [47] Q. L. Vuong, S. Van Doorslaer, J. L. Bridot, C. Argante, G. Alejandro, R. Hermann, S. Disch, C. Mattea, S. Stapf, Y. Gossuin, *Magn. Reson. Mater. Phys. Biol. Med.* **2012**, *25*, 467.
- [48] A. Nyman, M. Behm, G. Lindbergh, *Electrochim. Acta* **2008**, *53*, 6356.
- [49] J. Zhu, M. Yanilmaz, K. Fu, C. Chen, Y. Lu, Y. Ge, D. Kim, X. Zhang, *J. Membr. Sci.* **2016**, *504*, 89.